

Chapter 2

A Scalable Fluctuating Distance Field: An Application to Tumor Shape Analysis

R. Alp Guler, Andac Hamamci, and Gozde Unal

Abstract Tumor growth involves highly complicated processes and complex dynamics, which typically lead to deviation of tumor shape from a compact structure. In order to quantify the tumor shape variations in a follow-up scenario, a shape registration based on a scalable fluctuating shape field is described. In the earlier work of fluctuating distance fields (Tari and Genctav, J Math Imaging Vis 1–18, 2013; Tari, Fluctuating distance fields, parts, three-partite skeletons. In: Innovations for shape analysis. Springer, Berlin/New York, pp 439–466, 2013), the shape field consists of positive and negative values whose zero crossing separates the central and the peripheral volumes of a silhouette. We add a non-linear constraint upon the original fluctuating field idea in order to introduce a “fluctuation scale”, which indicates an assumption about peripherality. This provides the induction of an hierarchy hypothesis onto the field. When fixed, the field becomes robust for scale changes for analysis of correspondence. We utilize the scalable fluctuating field first in segmentation of the protruded regions in a tumor, which are significant for the radiotherapy planning and assessment procedures. Furthermore, the unique information encoded in the shape field is utilized as an underlying shape representation for follow-up registration applications. The representation performance of the scalable field for a fixed ‘fluctuation scale’ is demonstrated in comparison to the conventional distance transform approach for the registration problem.

2.1 Introduction

Tumor growth modeling is extensively studied using theoretical and experimental approaches by a variety of disciplines. While majority of the current studies are focused on modeling microscopic phenomena, mathematical models that operate

R.A. Guler (✉) • A. Hamamci • G. Unal

Faculty of Engineering and Natural Sciences, Sabanci University, Istanbul, Turkey

e-mail: alpuler@sabanciuniv.edu; andachamamci@sabanciuniv.edu;

gozdeunal@sabanciuniv.edu

at a macroscopic level are increasingly investigated through the analysis of clinical medical images [23]. Inhomogeneous and anisotropic tumor growth mechanisms lead to deviations of the tumor's shape characteristics from a compact structure and include protrusions. It is clear that extracting and quantifying the spatial information that irregular tumor shape parts carry would be a helpful macroscopic research tool for a better understanding of the dynamics of tumor growth.

As for clinical usage, the quantification and segmentation of the protruded and peripheral tumor regions could play an important role in radiosurgical applications. The goal of radiosurgery is to deliver a necrotic dose of radiation to the tumor while minimizing the amount of radiation to healthy brain tissues, especially to dose-sensitive tissues [39]. Series of beam configurations are determined as an optimization problem for treatment planning process such that beams will intersect to form a high dose at the tumor ROI. The rapid decrease at the edges of the radiation beam, which corresponds to the between 80 and 20 % isodose lines, is called the penumbra region and is generally located on the peripheral regions of the tumor [22]. A model that allows the distinguished analysis of the peripheral regions and segmentation of these parts that receive less radiation dose would not only be useful for isodose planning, but also for evaluating the success of the operation on protrusions and peripheral regions that are in close relation to critical anatomical structures. We propose an interactive method to distinguish protruded-peripheral parts using solely distance relations.

Segmentation or partitioning of shapes as boundary meshes is a problem of great interest for geometric modeling and computer graphics fields. The partitioning of the object represented by the mesh into meaningful parts, referred to as *part-type segmentation* by Shamir[33], is highly motivated by the study of human cognition [4, 18]. For an in-detail analysis of existing mesh segmentation methods we refer to [10, 33], along with recent successful approaches [16, 21] and a comparison of part-type segmentation techniques can be found in [1]. Distance functions described on the shape surfaces are commonly utilized for shape decomposition. There is a variety of surface metrics, e.g. geodesic [14], isophotic [24, 31], diffusion [11–13], volumetric part aware [25]. Though successful with a mesh representation, adaptation of these decomposition methods that use distance metrics to a volumetric representation would not be plausible. Additionally, partitioning the protrusions of tumors would require the abstraction of peripheral regions beforehand, else the association of partitioned boundary segments to the tumor volume would not be possible.

A sound approach for regional shape partitioning is utilizing the medial axis of symmetry, i.e. skeleton representation [6]. Partitioning shapes by associating regions with medial locus branches is very common and also successfully utilized in medical imaging [20, 30, 34, 35]. However, skeletal representations commonly suffer from certain instabilities. One of the instabilities is due to boundary perturbations, which are commonly addressed using smoothing or branch pruning approaches, which involve discarding branches that contribute little to the reconstruction of the shape [3, 7, 32]. For partitioning, choice of branches to prune would affect the resulting decomposition drastically considering the highly compact shapes of tumors, which

also tend to inherit symmetries. Another kind of instability occurs in the regions near the junctions, which is mainly referred to as the ligature problem [2, 5]. A variety of methods have been proposed to cope with the ligature problem, including detecting transitional areas [28], a Bayesian formulation for estimating likely branches that would produce the shape [15] or disconnected skeleton approaches [9, 26, 38]. Additional to these inconsistencies, the association of branches with protrusions is not straightforward and even under slight deformation the abstraction of the centrality of the shape is not possible for fold-symmetry cases, which are highly possible for tumor shapes. Tari’s model of Three-Partite-Skeleton, which arises from fluctuating distance fields [36] addresses this problem, which is highly motivating for the purpose of protrusion segmentation.

The fluctuating distance field [36, 37] contains both positive and negative values, and its zero crossing separates central and peripheral volumes. The maximum value of the field can be considered as a rough approximation of the center point for the shape in question, for instance the tumor, whereas the local minima correspond to rough approximations of center points for the protruded parts on the shape. The level curves encode the spatial relationships so explicitly that the separate protruded parts can be segmented even using a watershed segmentation without any additional processing. The extracted central region is compact and the peripheral region is always partitioned, unless it is a perfect annulus. In this model, no control exists over the ratio of region cardinality of positive field values to that of the negative field values. However, such a property can be an advantage in forming a shape field that respects a certain scale of central to peripheral regions of the shape. Particularly for shapes of tumorous structures, where boundaries between peripherality versus centrality is rather vague, variation of such a scale will introduce a flexibility in following shape analysis stages.

In this paper, we describe a scalable fluctuating distance field as a tumor description model. This model allows the user to interactively adjust the ratio of positive and negative domain sizes. The corresponding parameter can be set according to nature of the application. Thanks to this addition, a hierarchy of parts is not to be abstracted from the field as in [37]. Instead, fields that represent different hierarchical assumptions are formed, with the trade-off of losing linearity of the formulation. Details about the formulation and implementation of the shape field will be described in Sect. 2.2, where the fluctuation scale space that arises with the new parameter is introduced and exemplified on 2D shapes and 3D tumor volumes.

The constructed shape fields will be used for an alignment of baseline and follow-up tumor structures. In this registration problem, the distance transform is often used as a shape representation that describes the spatial relationships within the moving and fixed shapes [29]. The adjustment of the location of the zero-level set of the new distance field impairs the effect of scale changes to the resulting field for a fixed fluctuation scale, making the field a robust underlying shape representation for registration purposes. The registration process is described in Sect. 2.3 and experiments using both synthetic data and patient data are evaluated in Sect. 2.3.1, where the scalable fluctuating distance representation is compared to the conventional distance transform representation.

2.2 Scalable Fluctuating Distance Field

The concept of fluctuating distance fields, introduced by Tari [37], involves the exploitation of local and global spatial interactions to achieve a field that consists of both negative and positive values. The zero-level set partitions the shape domain into Ω^+ and Ω^- , which corresponds to the central region, a coarse and compact shape, and the peripheral region, which includes all the protrusions of the tumor, respectively. The ridge points on the surface yields the Three-Partite skeletons indicated. Our main motivation in using the fluctuating distance field is the information inherently coded in the resulting level curves at the peripheral regions, which will allow the explicit treatment to peripheral regions for further analysis. In this section we will describe our modification of this method, which will provide the required flexibility and interactivity for our purpose. We will follow by introducing the arising scale-space and illustrating segmented protruded parts using different fluctuation scales for 2D shapes and 3D tumor volumes.

The fluctuating distance field, $\omega: \Omega \rightarrow \mathbb{R}$ is a real valued function on a discrete lattice, $\Omega \subset \mathbb{Z} \times \mathbb{Z} \times \mathbb{Z}$, with a neighborhood system, \mathcal{N} . ω is generated by the minimization of linear combinations of regional and boundary energies, which are described over the shape domain Ω , as a function of ω .

2.2.1 Energy Terms

The regional energy consists of local and global terms that function as spatial regularizers. Tari [37] proposed a global regional energy, which is the squared average over the domain, connecting all the nodes using a global mean constraint:

$$E_{Global}(\omega_{i,j,k}) = \frac{1}{|\Omega|} \sum_{(l,m,n) \in \Omega} \omega_{l,m,n}^2 \quad (2.1)$$

Differentiating $E_{Global}(\omega_{i,j,k})$ over Ω leads to the following expression:

$$\frac{\partial E_{Global}(\omega_{i,j,k})}{\partial(\omega_{i,j,k})} = \frac{2}{|\Omega|} \sum_{(l,m,n) \in \Omega} \omega_{l,m,n} \quad (2.2)$$

which would be minimized if ω is composed of all zeros or is a fluctuating function, where positive and negative values cancel each other.

The local regional energy functions as a smoothness term. We use the sum of squared differences between neighboring pixels in a six neighborhood system, $\mathcal{N}(i, j, k)$ to obtain the required spatial smoothness for the ω field:

$$E_{Local}(\omega_{i,j,k}) = \sum_{(l,m,n) \in \mathcal{N}(i,j,k)} (\omega_{l,m,n} - \omega_{i,j,k})^2 \quad (2.3)$$

Differentiating this energy w.r.t $\omega_{i,j,k}$ results in the following expression, where \mathbb{L} corresponds to the seven-point discretization of the Laplacian operator:

$$\begin{aligned} \frac{\partial E_{Local}(\omega_{i,j,k})}{\partial(\omega_{i,j,k})} &= -2(\omega_{i+1,j,k} + \omega_{i-1,j,k} + \omega_{i,j+1,k} + \omega_{i,j-1,k} \\ &\quad + \omega_{i,j,k+1} + \omega_{i,j,k-1} - 6\omega_{i,j,k}) \\ &= -2\mathbb{L}(\omega_{i,j,k}) \end{aligned} \quad (2.4)$$

The boundary energy is defined for formulating the interactions along the level surfaces. The preservation of interactions between the nodes is imposed on the ω field using the usual distance transform as a bridge [37]. Thanks to this constraint, central regions of the shape, where the distance transform has larger values have much higher tendency to get positive ω values. The similarity to the distance transform function is formulated as follows:

$$E_{Bdry}(\omega_{i,j,k}) = (\omega_{i,j,k} - \mathcal{D}_{i,j,k})^2 \quad (2.5)$$

where \mathcal{D} denotes the distance transform of the shape. The derivative of E_{Bdry} w.r.t $\omega_{i,j,k}$ is then given as follows:

$$\frac{\partial E_{Bdry}(\omega_{i,j,k})}{\partial(\omega_{i,j,k})} = 2(\omega_{i,j,k} - \mathcal{D}_{i,j,k}) \quad (2.6)$$

Minimization of the combination of these energies results in a ω field that has low expected value, thus fluctuating (2.2), locally smooth (2.4) and resembling the distance transform of the shape (2.6).

2.2.2 A Sign Constraint to Control Fluctuation Scale

The natural location of the zero-level curve under the given constraints often becomes too close to the tumor boundaries, turning out to be a disadvantage while estimating a deformation between two ω fields. In addition, the ability to control the location of the zero crossing turns the ω field to a robust feature for an interactive tool for segmenting the protrusions on the tumor. Therefore we describe an additional global constraint to adjust the position of the zero crossing. The term is constructed as a quadratic expression forcing the sum of the signs of all nodes to be close to a predetermined ratio of the domain size, $|\Omega|$:

$$E_{Sign}(\omega_{i,j,k}) = \sum_{(i,j,k) \in \Omega} \left(\left(\sum_{(l,m,n) \in \Omega} sign(\omega_{l,m,n}) \right) - \eta |\Omega| \right)^2 \quad (2.7)$$

where $\eta \in [-1, 1]$ corresponds to the ratio of the intended sum of the signs of all ω points to the number of points in the shape domain $|\Omega|$. While minimizing (2.7), η is chosen as the desired ratio of:

$$\eta = \frac{\sum_{(l,m,n) \in \Omega} sign(\omega_{l,m,n})}{|\Omega|} = \frac{|\Omega^+| - |\Omega^-|}{|\Omega^+| + |\Omega^-|} \quad (2.8)$$

Differentiating this energy w.r.t. $\omega_{i,j,k}$ would give:

$$\frac{\partial E_{Sign}(\omega_{i,j,k})}{\partial(\omega_{i,j,k})} = 4 \sum_{(i,j,k) \in \Omega} \left(\left(\sum_{(l,m,n) \in \Omega} sign(\omega_{l,m,n}) \right) - \eta |\Omega| \right) \cdot \delta(\omega_{i,j,k}) \quad (2.9)$$

For the approximation of the signum function in a differentiable manner, we used a regularized Heaviside function, then the impulse function $\delta(z)$ was approximated as the derivative of $H(z)$:

$$sign(z) = 2H(z) - 1 \simeq \frac{2}{\pi} \arctan\left(\frac{z}{\epsilon}\right), \quad \delta(z) \simeq \frac{1}{\pi} \left(\frac{1}{1 + \left(\frac{z}{\epsilon}\right)^2} \right) \left(\frac{1}{\epsilon} \right) \quad (2.10)$$

where ϵ determines the steepness of the smoothed step and the impulse functions.

2.2.2.1 Formulation

The computation of ω is achieved by calculating the steady state solution to the linear combinations of the energy derivatives, which are described above. The combination of the energies is presented in a continuous formulation as follows:

$$\begin{aligned} & \iiint_{\Omega} (\omega_{x,y,z} - \mathcal{D}_{x,y,z})^2 + \left(\frac{1}{|\Omega|} \iiint_{\Omega} \omega(\alpha, \beta, \theta)^2 d\alpha d\beta d\theta \right) + (\nabla \omega(x, y, z))^2 + \dots \\ & \dots \left(\left(\iiint_{\Omega} sign(\omega_{\alpha,\beta,\theta}) d\alpha d\beta d\theta \right) - \eta |\Omega| \right)^2 dx dy dz \end{aligned} \quad (2.11)$$

The solution is obtained by applying the method of gradient descent in the following expression:

$$\frac{\partial \omega_{i,j,k}(\tau)}{\partial(\tau)} = - \frac{\partial(\beta_1 E_{Local}(\omega_{i,j,k}) + \beta_2 E_{Global}(\omega_{i,j,k}) + \gamma E_{Sign}(\omega_{i,j,k}) + \beta_3 E_{Bdry}(\omega_{i,j,k}))}{\partial \omega_{i,j,k}}$$

where β and γ values are Lagrange multipliers for the given energies. As natural choices, $\beta_1, \beta_2, \beta_3$ parameters can be interpreted as 1 [37]. γ is the only Lagrange multiplier that calibrates the relationship between the values of $E_{Bdry}(\omega_{i,j,k})$ and $E_{Sign}(\omega_{i,j,k})$. γ only affects convergence speed when it is within appropriate limits, that is not larger than the maximum value of the \mathcal{D} . We choose it as a normalization to the E_{Sign} of the ω field with the desired size of $|\Omega^+|$ using roughly a spherical zero-level set assumption. The iterative scheme on ω is revealed after an artificial time discretization in τ :

$$\begin{aligned} \frac{\omega_{i,j,k}^{n+1} - \omega_{i,j,k}^n}{\Delta \tau} = & \mathbb{L}(\omega_{i,j,k}) - \frac{1}{|\Omega|} \sum_{(i,j,k) \in \Omega} \omega_{i,j,k}^n - \left(\frac{1}{|\Omega|} \omega_{i,j,k}^n - \mathcal{D}_{i,j,k} \right) \\ & - \gamma \sum_{(i,j,k) \in \Omega} \left(\sum_{(i,j,k) \in \Omega} \text{sign}(\omega_{i,j,k}^n) - \eta |\Omega| \right) \delta(\omega_{i,j,k}^n) \quad (2.12) \end{aligned}$$

For the third term above, as ω is calculated up to a scale, a weight of $1/|\Omega|$ is used as a weighting between the \mathcal{D} and the ω field.

2.2.3 A Space of Fluctuation Scales

The effect of the parameter η of the E_{Sign} term is not only to change the location of the zero-level set. Its combination with the zero-mean constraint changes the encoding characteristics of the whole domain. For instance, positive η values force the negativity of the nodes that belong to Ω^- much more compared to $\eta = 0$ to satisfy the zero mean constraint. The reason is that there are less number of nodes that are negative, so those have to be more negative to satisfy the zero mean condition. The opposite goes for the negative η values. This causes a diversity in the characteristics of the fields as η changes. A separate normalization can be applied to the positive and negative parts of the fields, which diminishes this effect if not desired.

We depict the resulting fluctuation scale-space for a hand shape in Fig. 2.1a, where $\omega(\tilde{x}, \eta)$ is presented for \tilde{x} on a vertical line on the hand shape domain and the surface plot for the zero-crossing contour as a function of η is presented in (b).

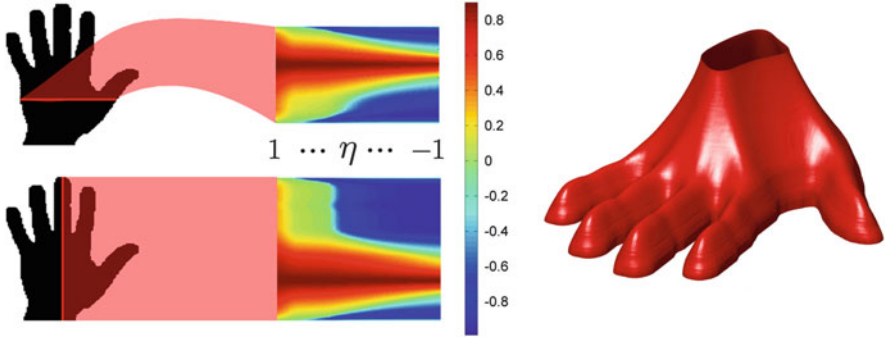


Fig. 2.1 (a) The normalized field $\omega(x = \tilde{x}, \eta)$, where \tilde{x} is shown by horizontal (*top*) and vertical (*bottom*) red lines. Image obtained by sweeping η from 1 to -1 . (b) Surface plot for $\omega(x, y, \eta) = 0$

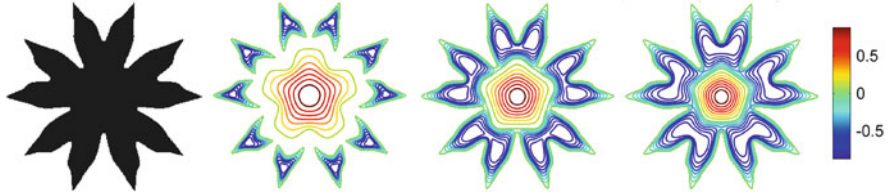


Fig. 2.2 From left to right: Input shape, ω for $\eta > 0$, ω for $\eta = 0$, ω for $\eta < 0$

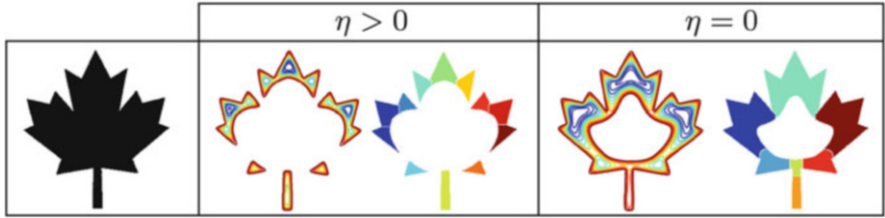


Fig. 2.3 Ω^- domain and watershed segmentation results for: *left* $\eta > 0$, *right* $\eta = 0$

Notice that the zero-level set sweeps the whole domain smoothly from boundary to central regions, as the information regarding Ω is encoded for different scales of peripherality.

The computed field is shown for three different η values (> 0 , $= 0$, < 0) for the symmetric shape silhouette in Fig. 2.2. Note that there are two levels of hierarchy in the peripheral regions of the shape, which can be seen as five different parts at a coarser level, later which are further differentiated into two separate parts. Varying the fluctuation scale parameter, one can capture those two levels of scale (coarser and finer) as can be observed in the resulting field with positive and negative η values, respectively.

A similar effect is achieved for the leaf silhouette in Fig. 2.3. Using a simple watershed segmentation [27], the resulting partitions reveal the three main leaves

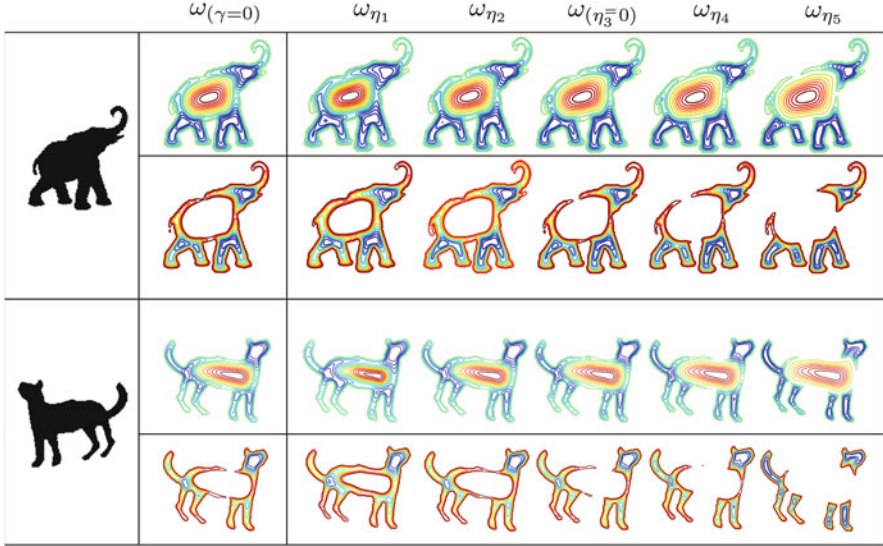


Fig. 2.4 The original ω field (left) [37], where the Lagrange multiplier γ is chosen as zero in Eq. 2.12 and five ω fields (right) calculated using increasing values for η , where $\eta_1 < \eta_2 < \eta_3 = 0$ and $\eta_5 > \eta_4 > \eta_3 = 0$. Upper row for both shapes is a contour plot of normalized ω and bottom rows depict ω for solely Ω^-

with $\eta = 0$, whereas the partitioning with the $\eta > 0$ field reveals the smaller protrusions on those three leaves. Here, the encoding of coarse to fine shape details nicely demonstrates the hierarchical aspect introduced into the fluctuating distance field.

We show the original w field and the scalable w field for various η values in Fig. 2.4 for an elephant and a cat silhouette. The first columns next to the silhouettes show the original field followed by the fields with increasing values of the fluctuation scale. The top picture is the whole w field, whereas the lower depicts only its Ω^- partition. Looking at the details at the legs of the fields more closely, for instance, the elephant's both front legs are merged in the original w field, as well as for the scalable field for smaller η values. When η is increased (e.g. see the rightmost field), the legs are separated, as can be observed in the Ω^- -part of the field. This is because where the two legs are joined, there is a single local maximum with the original and low scale parameter fields, whereas there are two separate local maxima for each leg with the high-scale-parameter field. The same observation holds for the various shape fields over the cat. Note the rear-most leg of the cat and its tail which share a joint single maximum, whereas that extremum separates into two separate maxima for the tail and the rear leg towards the higher η -scale. Another point to remark over these experiments is the interesting feature of the low- η -fields when compared to the original w -field. Note the cat's front legs, and elephant's rear legs, which seem to have a separate maximum for each leg in the

original shape field. However, the low η shape fields facilitate to peek at those same features first jointly then separately as the fluctuation scale varies from low to high. As these experiments demonstrate, the hierarchy over the shape is not built from the w -field as in [36], however, we modify the field itself to create the hierarchy that is sought for.

2.2.4 Interactive Tumor Protrusion Segmentation

The segmentation of the protruded tumor regions is achieved using the information in the negatively-valued regions of the ω field, which encapsulates local minima that depicts separate protrusions. The tumor should be segmented prior to the calculation of ω , for this purpose we use the Tumor-Cut method [17]. A contrast enhanced T1 MRI axial slice is depicted in Fig. 2.5, along with the ω field calculated on the tumor shape domain. Partitioning of the negatively-valued domain into protruded parts can be performed using the watershed transform [27] on the Ω^- field. The parts segmented from the resulting ω field can be observed Fig. 2.6 for a sample 3D tumor volume.

With the flexibility that E_{Sign} provides, the size of the positive compact part Ω^+ can be adjusted with user interference by medical experts or can be calculated

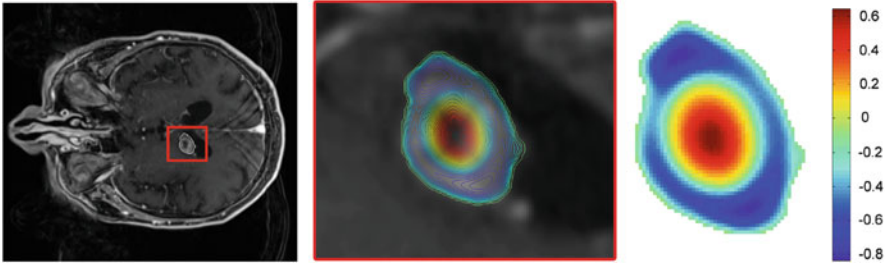


Fig. 2.5 *Left:* An axial slice of contrast enhanced T1 MRI of a patient with a tumor. *Middle:* ω field isocontours for the corresponding tumor slice. *Right:* ω field visualized

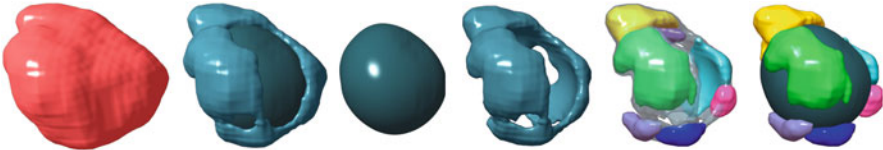


Fig. 2.6 *From left to right:* Tumor volume. Positive and negative parts of the proposed field. Positive part of the field. Negative part of the field. Segmented protrusions of the tumor enveloped in the negative part of the field. Segmented protrusions visualized with the positive part of the field

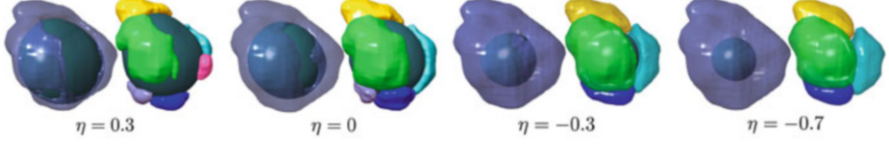


Fig. 2.7 Visualizations of positive(opaque) and negative(transparent) parts of the tumor field paired with corresponding segmentation results. The fluctuating distance field for each pair were generated using the corresponding η value

automatically by relaxing the η parameter until a predetermined hypothesis regarding the separated volumes are satisfied. The effect of η parameter on the resulting protruded parts is presented in Fig. 2.7.

2.3 Tumor Follow-Up Registration Using ω Fields

In order to obtain a valid and unbiased comparison between the performances of ω field and the conventional distance transform \mathcal{D} as underlying shape representations, we chose attributes that are essential in many of the registration algorithms that were proposed to calculate such deformations and combine them to end up with a basic yet powerful registration routine.

As linear data terms are not capable of performing well in case of large displacements, we used non-linear data terms and a coarse to fine warping approach which is a well studied combination in the area of optical flow estimation [8]. We follow the traditional model, formulated by means of an energy optimization problem, where deformation is calculated as a mapping between domains of shape fields ω_1 and ω_2 . The displacement field $u \in \mathbb{R}^3 = (u_1, u_2, u_3)$ describes the deformation between the tumor and the follow-up shape domains: $u : \Omega_1 \in \mathbb{R}^3 \rightarrow \Omega_2 \in \mathbb{R}^3$. In the following: $x \in \mathbb{R}^3 = (x_1, x_2, x_3)$. The assumption of constancy of the underlying shape representation is formulated as:

$$\omega_1(x) - \omega_2(x + u) = 0$$

In addition to this data term, a regularization term based on the gradient of the deformation field is utilized. Following the original Horn and Schunck optical flow model [19], the combined functional F , where α is a parameter that controls the smoothness term:

$$F(u) = \int_{\Omega_1} (\omega_1(x) - \omega_2(x + u))^2 + \alpha^2 (|\nabla u_1|^2 + |\nabla u_2|^2 + |\nabla u_3|^2) dx \quad (2.13)$$

is minimized to yield the Euler-Lagrange equations, which are non-linear due to the $\omega_2(x + u)$ terms they contain. The first order Taylor expansions are used for

those terms to obtain the linear system of three equations. First one of those three equations (for each coordinate) is written as:

$$(\omega_1(x) - \omega_2(x + u) - \nabla \omega_2(x + u) du) \omega_{2_{x_1}} + \alpha^2 \text{div}(\nabla u_1) = 0 \quad (2.14)$$

where $\omega_{2_{x_i}}$ is the spatial derivative of ω_2 w.r.t x_i and $du \in \mathbb{R}^3$ describes an unknown update to the known variable u . In its solution, we adopted the warping scheme, introduced in [8], where the deformation field u is set to zero at the coarsest level and updated by $u^{n+1} = u^n + du$, as soon as du is computed at each finer scale using an inner loop of SOR iterations. $\omega_2(x + u)$ is computed at the beginning of each outer iteration by applying a warping process to $\omega_2(x)$ using the deformation field, u^n . The number of outer iterations depends on the downsampling factor. In order to achieve the full potential of the model, instead of the conventional 0.5 downsampling factor, we used a fixed value of 0.95 and a large number of outer iterations.

2.3.1 Registration Results and Discussion

Using both 2D synthetic shapes and real patient 3D tumor volumes, the performance of the ω field as an underlying shape representation for tumor follow-up registration is demonstrated against the distance transform, which is the conventional method to impose spatial shape relationships to the registration procedure.

Synthetic data results for pre-smoothed distance transform, pre-smoothed normalized distance transform and fluctuating distance fields are respectively demonstrated in Fig. 2.8. On the top row for each of the experiments, the white and gray shapes denote the fixed and moving objects respectively, where the displacement vector field is demonstrated using arrows. Local volume change for each of the corresponding displacement field is generated using the determinant of the deformation gradient ($\det(I + \nabla_x u)$) and presented below. The values of the determinant that are greater than 1 indicate a local expansion, whereas values less than 1 indicate a local contraction.

The distance transform, \mathcal{D} is invariant to rotation and translation, but it is quite sensitive to scale changes[29]. Without a normalization, \mathcal{D} representation can perform well for deformations without scale changes only, which certainly is not the case for tumor followup analysis. On the other hand, normalization causes an ambiguity in the information preserved in \mathcal{D} , leading to an estimation of the deformation field that does not fully describe the change between the shapes. However the ω field adopts less ambiguity, since the information is partitioned to separate parts, which leads to a robust estimation of the deformation. E_{Sign} constraint contributes highly to this robustness to scale change, for the ratio η will be the same in Ω_1 and Ω_2 . Our experiments are highly coherent with this description. In Fig. 2.8, it is clear that \mathcal{D} without a normalization fails to produce a smooth vector field. In addition while the local volume change in the deformation fields

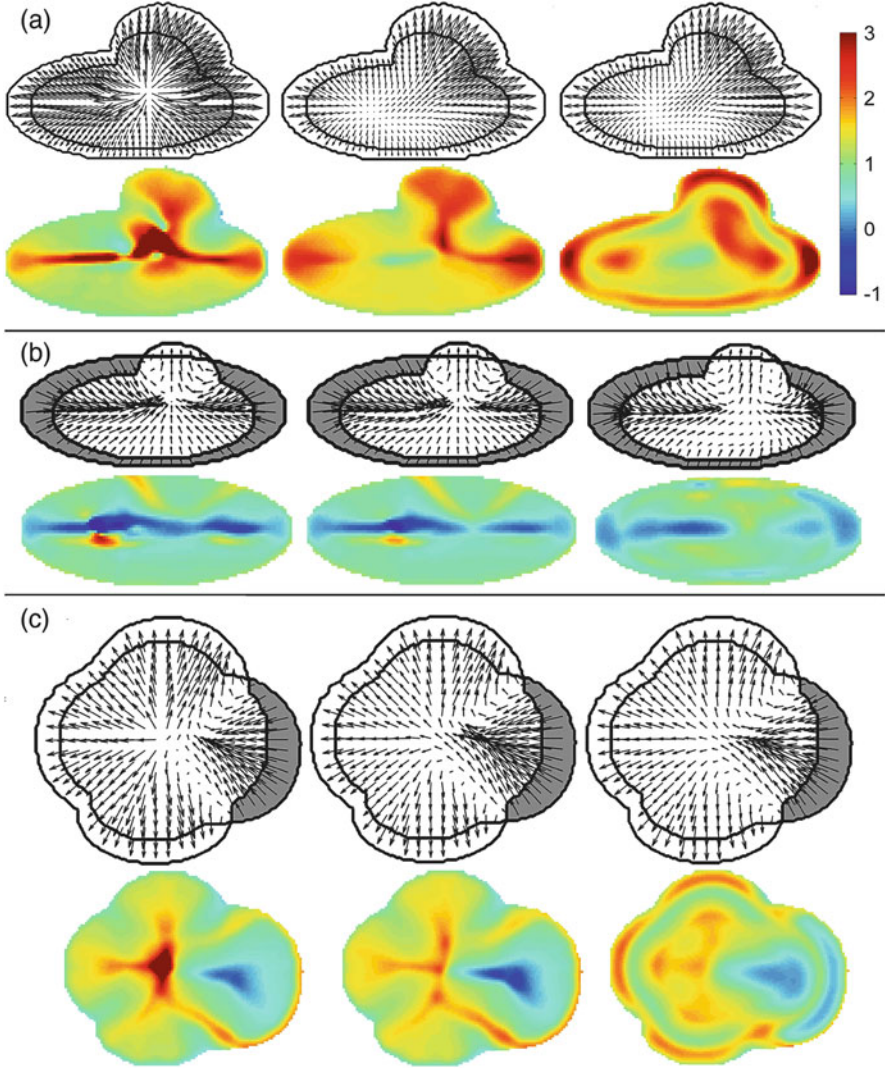


Fig. 2.8 (a–c): Visualizations of deformation field vectors and volume change pairs for registration of each synthetic shape couples, generated using *Left*: Distance transforms. *Middle*: Normalized High accuracy optical flow estimation based on a theory for warping distance transforms. *Right*: Scalable fluctuating distance fields

estimated using ω is in accordance with the change in the shapes, the normalized \mathcal{D} representation approaches fail to generate intuitive results. The expansions and contractions at the peripheral regions in Fig. 2.8 reveal the counter-intuitive nature of the displacement vectors generated using normalized \mathcal{D} .

Our experiments with patient data are demonstrated in Fig. 2.9, where the estimated 3D vector fields are visualized (on the left) for two pairs of tumor volumes

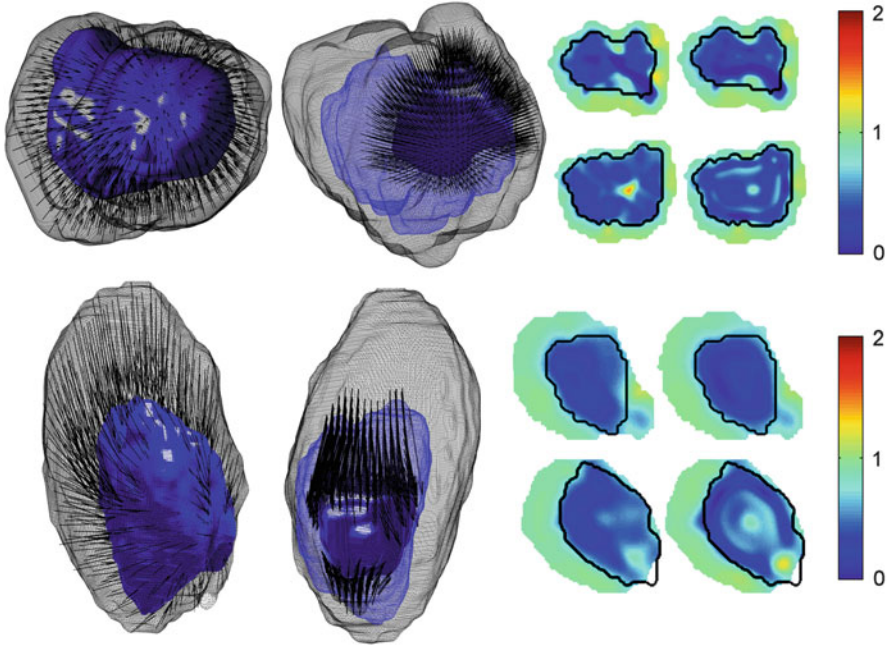


Fig. 2.9 For both parts of the figure: *Left:* Displacement field vectors from gray initial tumor to blue followup tumor. *Middle:* The displacement vectors to a specific segmented protrusion. *Right:* Local volume change maps in initial tumor domain for selected axial slices of the tumor shapes, the black contours denote the followup tumor. The maps on the left and right are generated from the deformation fields calculated using normalized \mathcal{D} and ω fields respectively

on each row. Those pairs of tumor volumes are obtained after a segmentation on a pre-therapy and follow-up MRI scan and undergo a large change in terms of global scale. In addition, we present the displacement fields to a specific protrusion (Fig. 2.9 in the middle), which was segmented as described in Sect. 2.2.4. Various 2D cross sections are also depicted on the right along with the local volume change maps using deformation gradient determinants as explained above. Considering the large motion, necessity of regularization is quite larger in 3D tumor volumes compared to the phantom data in Fig. 2.8. For that reason the differences in the volume change maps are not as distinctive for the 3D volumes. But when these subtle changes are analyzed, they reveal the strength of the ω field in contrast to \mathcal{D} . The volume change maps of the second tumor shape in Fig. 2.9 is a convincing example: When the upper slice is analyzed it is clear that the deformation calculated using ω field (on the right) describes the compression smoother, yet on the bottom slice (right), it successfully represents the expansion while the distance transform approach is too smooth to describe an expansion. A similar robust behavior can be observed on the given local volume changes of the first tumor pair in Fig. 2.9.

2.4 Conclusion

Motivated from physical significance and clinical relevance in follow-up problems, we proposed a method to analyze the protruded and peripheral regions of tumor shapes. In order to introduce a parameter to control the fluctuation scales, we modified the fluctuating distance field [37] with an additional constraint on the ratio of sizes of the positive and negative domains which indicate central and peripheral shape regions respectively. This modification led to an interactive framework for segmenting the protrusions and partitioning tumorous structures, albeit the loss of the linearity of the original shape field model. The introduced nonlinear term due to its variable scale parameter, i.e. the “fluctuation scale”, facilitates a hierarchical encoding of parts of the shape silhouette. By varying the fluctuation scale from low to high values, it is possible to observe the coarse to fine levels of hierarchy both in the field and its segmentations even by utilizing a very simple segmentation method.

The scalable shape field becomes a potentially powerful underlying shape representation for shape registration procedures, due to an increased robustness to scale changes without losing the information it inherits particularly in terms of the parts of a shape. For the registration application, the representation performance of the field was demonstrated in comparison to the conventional distance transform by observation of local volume changes in a tumor follow-up problem. Some counter-intuitive local changes were obtained by the latter, while the expected expansion and compression properties between pre-therapy and follow-up tumor volumes were provided by the deformation field estimated between the part-based shape fields.

References

1. Attene, M., Katz, S., Mortara, M., Patané, G., Spagnuolo, M., Tal, A.: Mesh segmentation-a comparative study. In: IEEE International Conference on Shape Modeling and Applications, SMI 2006, Matsushima, p. 7. IEEE (2006)
2. August, J., Siddiqi, K., Zucker, S.W.: Ligature instabilities in the perceptual organization of shape. In: IEEE Computer Society Conference on Computer Vision and Pattern Recognition, Fort Collins, vol. 2. IEEE (1999)
3. Bai, X., Latecki, L.J.: Path similarity skeleton graph matching. IEEE Trans. Pattern Anal. Mach. Intell. **30**(7), 1282–1292 (2008)
4. Biederman, I.: Recognition-by-components: a theory of human image understanding. Psychol. Rev. **94**, 115 (1987)
5. Blum, H., Nagel, R.N.: Shape description using weighted symmetric axis features. Pattern Recognit. **10**(3), 167–180 (1978)
6. Blum, H., et al.: A transformation for extracting new descriptors of shape. Models Percept. Speech Vis. Form **19**(5), 362–380 (1967)
7. Brady, M., Asada, H.: Smoothed local symmetries and their implementation. Int. J. Robot. Res. **3**(3), 36–61 (1984)
8. Brox, T., Bruhn, A., Papenbergh, N., Weickert, J.: High accuracy optical flow estimation based on a theory for warping. In: Computer Vision-ECCV 2004, Prague, pp. 25–36 (2004)
9. Burbeck, C.A., Pizer, S.M.: Object representation by cores: identifying and representing primitive spatial regions. Vis. Res. **35**(13), 1917–1930 (1995)

10. Chen, X., Golovinskiy, A., Funkhouser, T.: A benchmark for 3d mesh segmentation. *ACM Trans. Graph. (TOG)* **28**, 73 (2009). ACM
11. Coifman, R.R., Lafon, S.: Diffusion maps. *Appl. Comput. Harmon. Anal.* **21**(1), 5–30 (2006)
12. Crane, K., Weischedel, C., Wardetzky, M.: Geodesics in heat: a new approach to computing distance based on heat flow. *ACM Trans. Graph. (TOG)* **32**(5), 152 (2013)
13. De Goes, F., Goldenstein, S., Velho, L.: A hierarchical segmentation of articulated bodies. *Comput. Graph. Forum* **27**, 1349–1356 (2008). Wiley Online Library
14. Do Carmo, M.P., Do Carmo, M.P.: *Differential Geometry of Curves and Surfaces*, vol. 2. Prentice-Hall, Englewood Cliffs (1976)
15. Feldman, J., Singh, M.: Bayesian estimation of the shape skeleton. *Proc. Natl. Acad. Sci.* **103**(47), 18,014–18,019 (2006)
16. Golovinskiy, A., Funkhouser, T.: Consistent segmentation of 3d models. *Comput. Graph.* **33**(3), 262–269 (2009)
17. Hamamci, A., Kucuk, N., Karaman, K., Engin, K., Unal, G.: Tumor-cut: segmentation of brain tumors on contrast enhanced mr images for radiosurgery applications. *IEEE Trans. Med. Imaging* **31**(3), 790–804 (2012)
18. Hoffman, D.D., Richards, W.A.: Parts of recognition. *Cognition* **18**, 65–96 (1984)
19. Horn, B., Schunck, B.: Determining optical flow. *Artif. Intell.* **17**, 185–203 (1981)
20. Joshi, S., Pizer, S., Fletcher, P.T., Yushkevich, P., Thall, A., Marron, J.: Multiscale deformable model segmentation and statistical shape analysis using medial descriptions. *IEEE Trans. Med. Imaging* **21**(5), 538–550 (2002)
21. Kalogerakis, E., Hertzmann, A., Singh, K.: Learning 3d mesh segmentation and labeling. *ACM Trans. Graph. (TOG)* **29**(4), 102 (2010)
22. Khan, F.M.: *The Physics of Radiation Therapy*. Lippincott Williams & Wilkins, Philadelphia/London (2009)
23. Konukoglu, E., Pennec, X., Clatz, O., Ayache, N.: Tumor growth modeling in oncological image analysis. In: Bankman, I. (ed.) *Handbook of Medical Image Processing and Analysis* – New edition, chap. 18, pp. 297–307. Burlington, San Diego, London (2008)
24. Lai, Y.K., Zhou, Q.Y., Hu, S.M., Wallner, J., Pottmann, D., et al.: Robust feature classification and editing. *IEEE Trans. Vis. Comput. Graph.* **13**(1), 34–45 (2007)
25. Liu, R., Zhang, H., Shamir, A., Cohen-Or, D.: A part-aware surface metric for shape analysis. *Comput. Graph. Forum* **28**, 397–406 (2009). Wiley Online Library
26. Macrini, D., Dickinson, S., Fleet, D., Siddiqi, K.: Bone graphs: medial shape parsing and abstraction. *Comput. Vis. Image Underst.* **115**(7), 1044–1061 (2011)
27. Meyer, F.: Topographic distance and watershed lines. *Signal Process.* **38**(1), 113–125 (1994)
28. Mi, X., DeCarlo, D.: Separating parts from 2d shapes using relatibility. In: *IEEE 11th International Conference on Computer Vision, ICCV 2007, Rio de Janeiro*, pp. 1–8. IEEE (2007)
29. Paragios, N., Rousson, M., Ramesh, V.: Non-rigid registration using distance functions. *Comput. Vis. Image Underst.* **89**(2), 142–165 (2003)
30. Pizer, S.M., Fritsch, D.S., Yushkevich, P.A., Johnson, V.E., Chaney, E.L.: Segmentation, registration, and measurement of shape variation via image object shape. *IEEE Trans. Med. Imaging* **18**(10), 851–865 (1999)
31. Pottmann, H., Steiner, T., Hofer, M., Haider, C., Hanbury, A.: The isophotic metric and its application to feature sensitive morphology on surfaces. In: *Computer Vision-ECCV 2004, Prague*, pp. 18–23 (2004)
32. Shaked, D., Bruckstein, A.M.: Pruning medial axes. *Comput. Vis. Image Underst.* **69**(2), 156–169 (1998)
33. Shamir, A.: A survey on mesh segmentation techniques. *Comput. Graph. Forum* **27**, 1539–1556 (2008). Wiley Online Library
34. Styner, M., Gerig, G., Lieberman, J., Jones, D., Weinberger, D.: Statistical shape analysis of neuroanatomical structures based on medial models. *Med. Image Anal.* **7**(3), 207–220 (2003)
35. Styner, M., Lieberman, J.A., Pantazis, D., Gerig, G.: Boundary and medial shape analysis of the hippocampus in schizophrenia. *Med. Image Anal.* **8**(3), 197–203 (2004)

- 36. Tari, S.: Fluctuating distance fields, parts, three-partite skeletons. In: *Innovations for Shape Analysis*, pp. 439–466. Springer, Berlin/Heidelberg (2013)
- 37. Tari, S., Genctav, M.: From a non-local ambrosio-tortorelli phase field to a randomized part hierarchy tree. *J. Math. Imaging Vis.* **49**(1), 69–86. Springer (2014)
- 38. Tari, Z., Shah, J., Pien, H.: Extraction of shape skeletons from grayscale images. *Comput. Vis. Image Underst.* **66**(2), 133–146 (1997)
- 39. Tombropoulos, R., Schweikard, A., Latombe, J.C., Adler, J.: Treatment planning for image-guided robotic radiosurgery. In: *Computer Vision, Virtual Reality and Robotics in Medicine*, pp. 131–137. Springer, Berlin/Heidelberg (1995)

Research in Shape Modeling

Los Angeles, July 2013

Leonard, K.; Tari, S. (Eds.)

2015, XIV, 153 p. 94 illus., 81 illus. in color.,

ISBN: 978-3-319-16348-2